

Electrical impedance spectroscopy-based nondestructive testing for imaging defects in concrete structures

Habib Ammari[†] Jin Keun Seo[‡] Tingting Zhang[‡]
Liangdong Zhou[‡]

May 20, 2014

Abstract

An electrical impedance spectroscopy-based nondestructive testing (NDT) method is proposed to image both cracks and reinforcing bars in concrete structures. The method utilizes the frequency-dependent behavior of thin insulating cracks: low-frequency electrical currents are blocked by insulating cracks, whereas high-frequency currents can pass through the conducting bars without being blocked by thin cracks. Rigorous mathematical analysis relates the geometric structures of the cracks and bars to the frequency-dependent Neumann-to-Dirichlet data. Various numerical simulations support the feasibility of the proposed method.

Key words: Inverse problem, nondestructive testing, electrical impedance tomography, spectroscopic imaging, thin cracks, reinforcing bars, concrete structure

AMS subject classifications: 35R30, 35B30

1 Introduction

As a number of concrete structures currently in service reach the end of their expected serviceable life, nondestructive testing (NDT) methods to evaluate

[†]Department of Mathematics and Applications, Ecole Normale Supérieure, 45 Rue d'Ulm, 75005 Paris, France (habib.ammari@ens.fr).

[‡]Department of Computational Science and Engineering, Yonsei University, Seoul 120-749 Korea, (seoj@yonsei.ac.kr, zttouc@hotmail.com, zshould1990@hotmail.com).

their durability, and thus to ensure their structural integrity, have received gradually increasing attention. Concrete often degrades by the corrosion of the embedded reinforcing bars, which can lead to internal stress and thus to structurally disruptive cracks [16]. Various NDT techniques are currently used to monitor the reliability and condition of reinforced concrete structures without causing damage. They include impact-echo, half-cell potential, electrical resistivity testing, ground penetrating radar, ultrasonic testing, infrared thermographic techniques, and related tomographic imaging techniques [12, 13, 18, 26, 30, 31, 34]. Each technique has its intrinsic limitations in terms of reliability of defect detection, and the conventional techniques often depend on the subjective judgment of the inspectors. The limitations of existing methods have led to searches for more advanced visual inspection methods to detect invisible flaws and defects on the surface of concrete structures.

Electric methods such as electrical resistivity tomography (ERT) and electrical capacitance tomography (ECT) have been used to image cracks and steel reinforcing bars, which show clear electrical contrast from the background concrete. These electric methods can be used to complement acoustic methods by assessing different characteristics. They operate at low cost over long time periods. ERT and ECT employ multiple current sources to inject currents, and boundary voltages are then measured using voltmeters connected to multiple surface electrodes on the boundary of the imaging subject. These methods use the relationship between the applied current and the measured boundary voltage to invert the image of cracks and reinforcing bars. The methods suffer from a low defect location accuracy due to the ill-posedness of the corresponding inverse problem. In fact, the boundary current-voltage measurement alone may not be sufficient for robust identification of defects. Most of research outcomes had cooperated with some form of a prior information to deal with ill-posedness [4, 5, 6, 7, 10, 11, 14, 17, 20, 21, 22]. They suffer from low defect location accuracy owing to the ill-posed nature of the corresponding inverse problem. The boundary current-voltage measurement alone may not be sufficient for the robust identification of defects. Most of the previous methods can detect cracks and reinforcing bars when either only the crack or the bar exists in the concrete samples. Numerous experiments show that ERT or ECT applied with a single frequency struggle to identify both cracks and reinforcing bars when electrical currents are blocked by insulating cracks near the electrodes.

This paper focuses on electrical impedance spectroscopy-based NDT, viewing as an integrated ERT/ECT modality. It provides mathematical analysis to support a better method of visually inspecting defects in concrete structures. A thorough understanding of the frequency-dependent effects of

thin insulating cracks could be used to image cracks and reinforcing bars: low-frequency electrical currents are blocked by insulating cracks, whereas high-frequency currents can pass through the conducting bars without being blocked by thin cracks.

The mathematical analysis assumes that the background concrete is roughly homogeneous. The effective admittivity of the concrete could be regarded as roughly constant at coarse grid, despite it comprising a complex mixture of several materials. The proposed impedance-spectroscopy-based NDT method can provide visual assessment of the condition of a concrete structure, instead of coarse structure information, through tomographic images of the effective admittivity of the heterogeneous concrete structure.

In this paper, the cracks are modeled as thin inhomogeneities in the concrete, while the reinforcing bars are modeled as small inhomogeneities [1, 2, 3, 8, 9, 15]. Two operating frequency regimes are considered: low and high. Based on [23], the corresponding asymptotic expansion of the boundary voltage is established here at these two frequency regimes.

The main purpose is to show that multi-frequency impedance measurements can be used to visualize different objects. For simplicity, cracks are idealized as linear segments. The numerical simulations use a conventional 16-channel EIT system, with the electrical current applied between two adjacent electrodes at different frequencies. The boundary voltage data are then measured between two adjacent electrodes attached on the surface. Frequency-difference EIT reconstruction allows the detection of both the cracks and the reinforcing bars within the concrete structures. A variety of numerical experiments is presented here to illustrate the main findings.

2 Mathematical model

For rigorous analysis, we use the simplified two-dimensional model by considering axially symmetric cylindrical sections under the assumption that the out-of-plane current density is negligible in an imaging slice. We assume a two dimensional electrically conducting domain Ω with its connected C^2 -boundary Ω . We denote the conductivity distribution of the domain by σ and the permittivity distribution by ϵ . Inside Ω , there exist thin cracks \mathcal{C}_k , $k = 1, 2, \dots, N_C$ and reinforcing bars D_k , $k = 1, 2, \dots, N_D$ as shown in figure 1. Let $D = \cup_{k=1}^{N_D} D_k$ and $\mathcal{C} = \cup_{k=1}^{N_C} \mathcal{C}_k$ denote the collections of the reinforcing bars and cracks, respectively. Since the conductivity σ and permittivity ϵ change abruptly across the reinforcing bars and cracks, we

denote

$$\sigma(x) = \begin{cases} \sigma_c & \text{for } x \in \mathcal{C}, \\ \sigma_d & \text{for } x \in D, \\ \sigma_b & \text{for } x \in \Omega \setminus (D \cup \mathcal{C}), \end{cases} \quad \text{and } \epsilon(x) = \begin{cases} \epsilon_c & \text{for } x \in \mathcal{C}, \\ \epsilon_d & \text{for } x \in D, \\ \epsilon_b & \text{for } x \in \Omega \setminus (D \cup \mathcal{C}). \end{cases} \quad (2.1)$$

Because the cracks are highly insulating and the reinforcing bars are highly conducting, we consider the following two extreme contrast cases:

$$\frac{\sigma_c}{\sigma_b} \approx 0 \quad \text{and} \quad \frac{\sigma_d}{\sigma_b} \approx \infty.$$

The inverse problem is to identify the cracks \mathcal{C}_k and reinforcing bars D_k from measured current-voltage data in multi-frequency EIT system. In the frequency range below 1MHz ($\frac{\omega}{2\pi} \leq 10^6$), we inject a sinusoidal current $g(x)\sin(\omega t)$ at $x \in \partial\Omega$ where g is the magnitude of the current density on $\partial\Omega$ and $g \in H_\diamond^{-1/2}(\partial\Omega) := \{\phi \in H^{-1/2}(\partial\Omega) : \int_{\partial\Omega} \phi ds = 0\}$. The injected current produces the time-harmonic potential u^ω in Ω which is dictated by

$$\begin{cases} \nabla \cdot (\gamma^\omega(x) \nabla u^\omega(x)) = 0 & \text{in } \Omega, \\ \gamma^\omega \frac{\partial u^\omega}{\partial \nu} = g & \text{on } \partial\Omega, \end{cases} \quad (2.2)$$

where $\gamma^\omega = \sigma + i\omega\epsilon$, ν is the outward unit normal vector on $\partial\Omega$, and $\frac{\partial}{\partial \nu}$ is the normal derivative. Setting $\int_{\partial\Omega} u^\omega ds = 0$, we can obtain a unique solution u^ω to (2.2) from the Lax-Milgram theorem. Hence, we can define the Neumann to Dirichlet map $\Lambda_\omega : H_\diamond^{-1/2}(\partial\Omega) \rightarrow H_\diamond^{1/2}(\partial\Omega)$ by $\Lambda_\omega(g) = u^\omega|_{\partial\Omega}$. Using N_E -channel multi-frequency EIT system, we may inject N_E number of linearly independent currents at several angular frequencies $\omega_1, \dots, \omega_{N_\omega}$ and measure the induced corresponding boundary voltages. We collect these current-voltage data $\{\Lambda_{\omega_j}(g_k) : k = 1, \dots, N_E, j = 1, \dots, N_\omega\}$ at various frequencies ranging from 10Hz to 1MHz which will be used to detect cracks and reinforcing bars.

To carry out rigorous analysis, we will restrict our considerations to geometric structures of \mathcal{C} and D as shown in Figure 1. We assume that each crack \mathcal{C}_k has a uniform thickness of δ_k and is a neighborhood of a C^2 -smooth open curve \mathcal{L}_k :

$$\mathcal{C}_k = \{x + h\nu_x : x \in \mathcal{L}_k, -\delta_k < h < \delta_k\}, \quad (k = 1, 2, \dots, N_C). \quad (2.3)$$

The thickness to the crack length ratio is assumed to be very small, that is, $\delta_k \approx 0$. We also assume that each reinforcing bar has the form

$$D_k := z_k + \delta_D B_k, \quad (k = 1, 2, \dots, N_D), \quad (2.4)$$

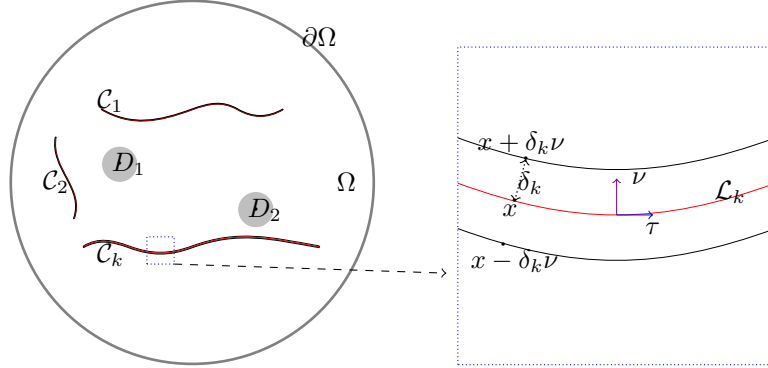


Figure 1: (left) Inside the domain Ω , there are highly insulating cracks \mathcal{C}_k and highly conducting D_k . (right) Crack \mathcal{C}_k has uniform thickness of δ_k .

where B_k is a bounded smooth reference domain centered at $(0, 0)$ and δ_D is related to the diameter of D_k .

We assume that \mathcal{C}_k and D_k are well separated from each other as well as the boundary $\partial\Omega$. To be precise, there exists a constant $d_0 > 0$ such that conditions:

$$\begin{aligned} \inf_{k \neq k'} \text{dist}(D_k, D_{k'}) &\geq d_0, & \inf_{k \neq k'} \text{dist}(\mathcal{C}_k, \mathcal{C}_{k'}) &\geq d_0, \\ \text{dist}(\mathcal{C}, \partial\Omega) &\geq d_0, & \text{dist}(D, \partial\Omega) &\geq d_0, & \text{dist}_{k,j}(\mathcal{C}_k, D_j) &\geq 2d_0. \end{aligned} \quad (2.5)$$

3 Asymptotic expansions

Since each crack \mathcal{C}_k is highly insulating with very thin thickness, there is a noticeable potential jump along the crack [1, 24] and the jump changes with frequency. In this part we will focus on analyzing the frequency-dependent behaviors of the complex potential around the cracks. For a better understanding, we present the electrical current flux at different frequency ranges in Figure 2. These figures clearly show how the electric current density changes with frequency in the presence of both concrete cracks and reinforcing bars.

3.1 Jump conditions

To understand the phenomenon described in Figure 2, we will start with investigating the jumps along sidewalls of concrete cracks by making use of Taylor expansion. By iterating the asymptotic formula for the crack, we can derive the leading-order term in the expansion of the boundary voltage when there are several well-separated cracks.

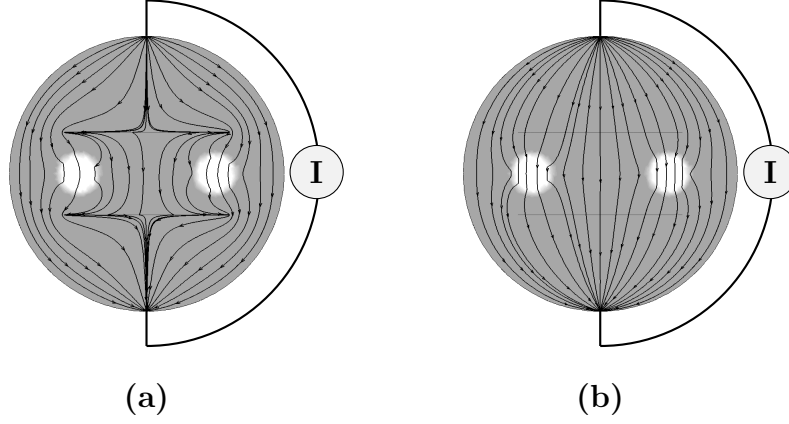


Figure 2: Electrical current flux for a concrete model with reinforcing bars (white) and cracks: (a) at low frequencies; (b) at high frequencies.

For notational convenience, we define exterior(+)/interior(-) normal derivative on the boundary of \mathcal{C}_k as follows:

$$\begin{aligned} \frac{\partial u^\omega}{\partial \nu}(x - \delta_k \nu_x)|_{\pm} &= \lim_{s \rightarrow 0^+} \frac{\partial u^\omega}{\partial \nu}(x - \delta_k \nu_x \mp s \nu_x), \\ \frac{\partial u^\omega}{\partial \nu}(x + \delta_k \nu_x)|_{\pm} &= \lim_{s \rightarrow 0^+} \frac{\partial u^\omega}{\partial \nu}(x + \delta_k \nu_x \pm s \nu_x) \end{aligned} \quad (x \in \mathcal{L}_k),$$

where ν is the unit normal vector to the curve \mathcal{L}_k as shown in Figure 1. Denote $[u^\omega]_k$ and $[\frac{\partial u^\omega}{\partial \nu}]_k$ as jump of potential and jump of normal derivative across the boundary of crack \mathcal{C}_k , respectively:

$$\begin{aligned} [u^\omega(x)]_k &:= u^\omega(x + \delta_k \nu_x) - u^\omega(x - \delta_k \nu_x) \\ [\frac{\partial u^\omega}{\partial \nu}(x)]_k &:= \frac{\partial u^\omega}{\partial \nu}(x + \delta_k \nu_x)|_+ - \frac{\partial u^\omega}{\partial \nu}(x - \delta_k \nu_x)|_+ \end{aligned} \quad (x \in \mathcal{L}_k).$$

Lemma 3.1. *For $x \in \mathcal{L}_k$, the potential u^ω and normal derivative $\frac{\partial u^\omega}{\partial \nu}$ satisfy the following jump relations across the thin crack:*

$$[u^\omega(x)]_k = 2\delta_k \frac{1}{\lambda_c(\omega)} \frac{\partial u^\omega}{\partial \nu}(x - \delta_k \nu_x)|_+ + O((\delta_k)^2), \quad (3.1)$$

and

$$\left[\frac{\partial u^\omega}{\partial \nu}(x) \right]_k = -2\delta_k \lambda_c(\omega) \frac{\partial^2 u^\omega}{\partial \tau^2}(x - \delta_k \nu_x) + O((\delta_k)^2), \quad (3.2)$$

where

$$\lambda_c(\omega) = \frac{\sigma_c + i\omega\epsilon_c}{\sigma_b + i\omega\epsilon_b}. \quad (3.3)$$

Proof. Using the transmission condition of the potential u^ω along the boundary of \mathcal{C}_k , we have for $x \in \mathcal{L}_k$

$$\begin{aligned} u^\omega(x + \delta_k \nu_x) &= u^\omega(x - \delta_k \nu_x) + 2\delta_k \frac{\partial u^\omega}{\partial \nu}(x - \delta_k \nu_x)|_- + O((\delta_k)^2), \\ &= u^\omega(x - \delta_k \nu_x) + 2\delta_k \frac{1}{\lambda_c(\omega)} \frac{\partial u^\omega}{\partial \nu}(x - \delta_k \nu_x)|_+ + O((\delta_k)^2). \end{aligned}$$

Similarly, we use the transmission condition along the crack and Taylor expansion to get

$$\begin{aligned} \frac{\partial u^\omega}{\partial \nu}(x + \delta_k \nu_x)|_+ &= \lambda_c(\omega) \frac{\partial u^\omega}{\partial \nu}(x + \delta_k \nu_x)|_- \\ &= \lambda_c(\omega) \left(\frac{\partial u^\omega}{\partial \nu}(x - \delta_k \nu_x)|_- + 2\delta_k \frac{\partial^2 u^\omega}{\partial \nu^2}(x - \delta_k \nu_x)|_- \right) + O((\delta_k)^2), \\ &= \frac{\partial u^\omega}{\partial \nu}(x - \delta_k \nu_x)|_+ - 2\lambda_c(\omega) \delta_k \frac{\partial^2 u^\omega}{\partial \tau^2}(x - \delta_k \nu_x) + O((\delta_k)^2), \end{aligned}$$

with τ the unit tangent vector with respect to $x \in \mathcal{L}_k$. \square

From the above asymptotic formulas (3.1) and (3.2), the jump of the potential and its normal derivative across the cracks depend on angular frequency ω as well as the thickness δ_k . Therefore, the multi-frequency Cauchy data (multi-frequency current-voltage data $\{\Lambda_{\omega_j}(g_k) : k = 1, \dots, N_E, j = 1, \dots, N_\omega\}$) reflects not only the geometry of cracks \mathcal{L}_k but also its thickness δ_k . This is the major advantage of multi-frequency EIT system over the other existing non-destructive testing system.

3.2 Effective zero-thickness crack model

Based on Lemma 3.1, we can describe an effective zero-thickness crack model by imposing the jump conditions of $[u^\omega]_k$ and $[\frac{\partial u^\omega}{\partial \nu}]_k$ on the curves \mathcal{L}_k . This means that the potential u^ω can be approximated by the corresponding potential \tilde{u}^ω satisfying the effective zero-thickness crack model [23, 28, 29]:

$$\left\{ \begin{array}{l} \nabla \cdot ((\gamma_b^\omega + (\gamma_d^\omega - \gamma_b^\omega)\chi_D)\nabla \tilde{u}^\omega) = 0 \quad \text{in } \Omega \setminus \cup_{k=1}^{N_C} \mathcal{L}_k, \\ [\frac{\partial \tilde{u}^\omega}{\partial \nu}]_{\mathcal{L}_k} = 0, \quad k = 1, 2, \dots, N_C, \\ [\tilde{u}^\omega]_{\mathcal{L}_k} = 2\delta_k \frac{1}{\lambda_c(\omega)} \frac{\partial \tilde{u}^\omega}{\partial \nu}|_+, \quad k = 1, 2, \dots, N_C, \\ \gamma_b^\omega \frac{\partial \tilde{u}^\omega}{\partial \nu} = g \quad \text{on } \partial\Omega, \end{array} \right. \quad (3.4)$$

where χ_D is the characteristic function of D and

$$\begin{aligned} [\tilde{u}^\omega(x)]_{\mathcal{L}_k} &:= \lim_{s \rightarrow 0^+} (\tilde{u}^\omega(x + s\nu_x) - \tilde{u}^\omega(x - s\nu_x)) \\ [\frac{\partial \tilde{u}^\omega}{\partial \nu}(x)]_{\mathcal{L}_k} &:= \lim_{s \rightarrow 0^+} \left(\frac{\partial \tilde{u}^\omega}{\partial \nu}(x + s\nu_x) - \frac{\partial \tilde{u}^\omega}{\partial \nu}(x - s\nu_x) \right) \quad (x \in \mathcal{L}_k). \end{aligned} \quad (3.5)$$

Since $u^\omega \approx \tilde{u}^\omega$ in $\{x \in \Omega : \text{dist}(x, \partial\Omega) < \frac{d_0}{2}\}$, the forward model (2.2) and the effective zero-thickness crack model (3.4) have basically the same Neumann-to-Dirichlet data in terms of the inverse problem. From now on, let u^ω denote a solution of (3.4) for notational simplicity. From the above zero-thickness crack model, the boundary condition along curve \mathcal{L}_k depends on thickness δ_k of concrete crack as well as the value of $\lambda_c(\omega)$ which is related with injected current frequency ω . The aim of the following few sections is to derive an explicit formula for detecting positions of reinforcing bars and cracks by using asymptotic expansions of u^ω . The explicit formula depends on injected frequency ω and crack thickness δ_k . We consider separately the following two cases[23]:

- High-frequency case: $\delta_k \approx 0$ and $0 < c_0 \leq |\lambda_c(\omega)|$.
- Low-frequency case: $|\lambda_c(\omega)| \approx 0$ and $\delta_k \approx 0$ with $|\lambda_c(\omega)|^{-1}\delta_k \approx \beta$ and $0 < \beta < \infty$.

3.3 High-frequency case: $\delta_k \approx 0$ and $0 < c_0 \leq |\lambda_c(\omega)|$

Let u_0 be the solution of equation (2.2) with $g = a \cdot \nu$ on $\partial\Omega$ and $\gamma^\omega = 1$, where a is a unit vector in \mathbb{R}^2 .

Denote the fundamental solution of Laplace equation in two dimension as $\Gamma(x, x')$:

$$\Gamma(x, x') := -\frac{1}{2\pi} \ln |x - x'|,$$

and define the trace operator $\mathcal{K}_\Omega[\phi]$ for $\phi \in L^2(\partial\Omega)$ by

$$\mathcal{K}_\Omega[\phi](x) := \frac{1}{2\pi} \int_{\partial\Omega} \frac{(x' - x) \cdot \nu(x')}{|x - x'|^2} \phi(x') ds_{x'}, \quad x \in \partial\Omega. \quad (3.6)$$

In high-frequency case, we suppose that the injected current frequency ω is not that low, so that $|\lambda_c(\omega)|$ is away from zero. When the thickness δ_k goes to zero, the potential jump along each crack \mathcal{C}_k also goes to zero according to lemma (3.1). Therefore the proposed problem can be regarded as traditional impedance boundary value problem and the influence of concrete crack on the high-frequency current-voltage data is very weak as shown in Figure 2(b).

In this case, the following boundary voltage asymptotic expansion holds at high-frequencies. For detailed analysis and similar proof, one may refer to [1, 8, 9, 15].

Theorem 3.2. *[Asymptotic expansion at high-frequencies] For $x \in \partial\Omega$, when the injection current frequency is high, the perturbations of voltage potential*

u^ω due to small inclusions D_k and thin inclusions \mathcal{C}_k can be expressed as

$$\begin{aligned} & \left(-\frac{1}{2}I + \mathcal{K}_\Omega \right) [u^\omega - u_0](x) \\ &= -\sum_{k=1}^{N_C} \int_{\mathcal{L}_k} \delta_k A_k(x', \lambda_c(\omega)) \nabla u_0(x') \cdot \nabla \Gamma(x, x') ds_{x'} \\ & \quad - \delta_D^2 \sum_{k=1}^{N_D} \nabla \Gamma(x, z_k) \cdot M(\lambda_d(\omega), B_k) \nabla u_0(z_k) + O(\delta_k^2) + O(\delta_D^3), \end{aligned} \quad (3.7)$$

where $A_k(x, \lambda_c(\omega))$ is a 2×2 symmetric matrix whose eigenvectors are $\nu_k(x)$ and $\tau_k(x)$ and the corresponding eigenvalues are $2(1 - \frac{1}{\lambda_c(\omega)})$ and $2(\lambda_c(\omega) - 1)$, respectively. And $M(\lambda_d(\omega), B_k)$ is polarization tensor given by

$$M_{ij} := \int_{\partial B_k} y^j (\lambda_d(\omega) I - \mathcal{K}_{B_k}^*)^{-1} (\nu_x \cdot \nabla x^i)(y) ds_y, \quad i, j = 1, 2, \quad (3.8)$$

with

$$\lambda_d(\omega) = \frac{(\sigma_d + \sigma_b) + i\omega(\epsilon_d + \epsilon_b)}{2((\sigma_d - \sigma_b) - i\omega(\epsilon_d - \epsilon_b))}. \quad (3.9)$$

Theorem 3.2 has obvious meaning that the measured boundary data is influenced by cracks and reinforcing bars since the first term on right-side of formula (3.7) only related with cracks while the second term only related with reinforcing bars. Depending on the magnitude of ω , δ_k and δ_D , the dominative term on right-side of formula (3.7) may be alternative. To see the effect of ω , δ_k and δ_D on the measured boundary data more clearly, we need further analysis on the expansion formula in Theorem 3.2.

Theorem 3.3 (Identification of cracks and bars). *Let $\lambda_c(\omega)$ and δ_k satisfy the conditions stated in high-frequency case. Assume that all the cracks are line segments and all the bars are disks. Let Q_k and P_k denote the endpoints of the segment \mathcal{L}_k and let z_k denote the center of D_k . Then $(-\frac{1}{2}I + \mathcal{K}_\Omega)[u^\omega - u_0]$ on the boundary $\partial\Omega$ can be expressed as*

$$\Re \left\{ \left(-\frac{1}{2}I + \mathcal{K}_\Omega \right) [u^\omega - u_0](\mathbf{x}) \right\} = \Re \{ G^{\Re}(\mathbf{x}) \} + O(\delta_k^2) + O(\delta_D^3), \quad (3.10)$$

$$\Im \left\{ \left(-\frac{1}{2}I + \mathcal{K}_\Omega \right) [u^\omega - u_0](\mathbf{x}) \right\} = \Im \{ G^{\Im}(x) \} + O(\delta_k^2) + O(\delta_D^3), \quad (3.11)$$

where G^{\Re} and G^{\Im} are meromorphic functions:

$$\frac{dG^{\Re}(\mathbf{x})}{d\mathbf{x}} = \sum_{k=1}^{N_C} \mathfrak{E}_k^{\Re}(\omega, \delta_k) \left(\frac{1}{\mathbf{x} - \mathbf{Q}_k} - \frac{1}{\mathbf{x} - \mathbf{P}_k} \right) - \sum_{k=1}^{N_D} \mathfrak{D}_k^{\Re}(\omega, \delta_D) \frac{1}{(\mathbf{x} - \mathbf{z}_k)^2} \quad (3.12)$$

$$\frac{dG^{\Im}(\mathbf{x})}{d\mathbf{x}} = \sum_{k=1}^{N_C} \mathfrak{E}_k^{\Im}(\omega, \delta_k) \left(\frac{1}{\mathbf{x} - \mathbf{Q}_k} - \frac{1}{\mathbf{x} - \mathbf{P}_k} \right) - \sum_{k=1}^{N_D} \mathfrak{D}_k^{\Im}(\omega, \delta_D) \frac{1}{(\mathbf{x} - \mathbf{z}_k)^2} \quad (3.13)$$

and

$$\mathfrak{E}_k^{\Re}(\omega, \delta_k) = \frac{\delta_k}{\pi} \left(\Re\{(\lambda_c(\omega) - 1)\} a_{\tau_k} + i \Re\left\{1 - \frac{1}{\lambda_c(\omega)}\right\} a_{\nu_k} \right) \quad (3.14)$$

$$\mathfrak{E}_k^{\Im}(\omega, \delta_k) = \frac{\delta_k}{\pi} \left(\Im\{\lambda_c(\omega) - 1\} a_{\tau_k} + i \Im\left\{1 - \frac{1}{\lambda_c(\omega)}\right\} a_{\nu_k} \right) \quad (3.15)$$

$$\mathfrak{D}_k^{\Re}(\omega, \delta_D) = -\Re\left\{ \frac{|B_k| \delta_D^2}{2\pi \lambda_d(\omega)} \right\} \mathbf{a}, \quad \mathfrak{D}_k^{\Im}(\omega, \delta_D) = -\Im\left\{ \frac{|B_k| \delta_D^2}{2\pi \lambda_d(\omega)} \right\} \mathbf{a}. \quad (3.16)$$

Here, $a_{\nu_k} = a \cdot \nu_k$, $a_{\tau_k} = a \cdot \tau_k$, $\mathbf{x} = x \cdot (1, i)$, $\mathbf{a} = a \cdot (1, i)$, $\mathbf{z}_k = z_k \cdot (1, i)$, $\mathbf{P}_k = P_k \cdot (1, i)$, and $\mathbf{Q}_k = Q_k \cdot (1, i)$.

Proof. Since B_k is a disk, the formula (3.8) gives $M(\lambda_d(\omega), B_k) = \frac{|B_k|}{\lambda_d(\omega)} I$. Hence, the formula (3.7) in Theorem 3.2 can be expressed as

$$\left(-\frac{1}{2} I + \mathcal{K}_\Omega \right) [u^\omega - u_0](x) = \Phi(x) + O(\delta_k^2) + O(\delta_D^3) \quad (x \in \partial\Omega), \quad (3.17)$$

where Φ is

$$\Phi(x) = - \sum_{k=1}^{N_C} \delta_k \int_{\mathcal{L}_k} (A_k a) \cdot \nabla \Gamma(x, x') ds_{x'} - \frac{\delta_D^2}{2\pi} \sum_{k=1}^{N_D} \frac{|B_k|}{\lambda_d(\omega)} \frac{x - z_k}{|x - z_k|^2} \cdot a. \quad (3.18)$$

We use $a = a_{\nu_k} \nu_k + a_{\tau_k} \tau_k$ to get

$$\begin{aligned} \Phi(x) = & -\frac{1}{2\pi} \sum_{k=1}^{N_C} \delta_k \int_{\mathcal{L}_k} \left(2\left(1 - \frac{1}{\lambda_c(\omega)}\right) a_{\nu_k} \nu_k + 2(\lambda_c(\omega) - 1) a_{\tau_k} \tau_k \right) \cdot \frac{x - x'}{|x - x'|^2} ds_{x'} \\ & - \frac{\delta_D^2}{2\pi \lambda_d(\omega)} \sum_{k=1}^{N_D} |B_k| \frac{x - z_k}{|x - z_k|^2} \cdot a \quad (x \in \partial\Omega). \end{aligned} \quad (3.19)$$

From now on, we shall identify \mathbb{R}^2 with the complex plane \mathbb{C} . In order to avoid confusion, we will adopt the following notations: $x = (x_1, x_2)$ denotes a

point in \mathbb{R}^2 and $\mathbf{x} = x_1 + ix_2$ will be the corresponding point in \mathbb{C} . Similarly, $x' = (x'_1, x'_2)$, $z_k = (z_{k_1}, z_{k_2})$, $a = (a_1, a_2)$ in \mathbb{R}^2 can be changed to $\mathbf{x}' = x'_1 + ix'_2$, $\mathbf{z}_k = z_{k_1} + iz_{k_2}$ and $\mathbf{a} = a_1 + ia_2$ in \mathbb{C} . Since $\lambda_c(\omega)$, $\lambda_d(\omega)$ as well as u^ω are complex, we will consider real and imaginary part of $\Phi(x)$ separately.

The real part of $\Phi(x)$ for $x \in \partial\Omega$ can be expressed as

$$\Re\{\Phi(\mathbf{x})\} = \Re \left\{ -\frac{1}{2\pi} \sum_{k=1}^{N_C} \delta_k \int_{\mathcal{L}_k} \frac{\boldsymbol{\xi}}{\mathbf{x} - \mathbf{x}'} ds_{\mathbf{x}'} - \Re \left\{ \frac{\delta_D^2}{2\pi\lambda_d(\omega)} \right\} \sum_{k=1}^{N_D} |B_k| \frac{\mathbf{a}}{\mathbf{x} - \mathbf{z}_k} \right\} \quad (3.20)$$

where $\boldsymbol{\xi} = \xi \cdot (1, i)$ and ξ is

$$\xi = \Re \left\{ 2 \left(1 - \frac{1}{\lambda_c(\omega)} \right) a_{\nu_k} \nu_k + 2(\lambda_c(\omega) - 1) a_{\tau_k} \tau_k \right\}. \quad (3.21)$$

Since \mathcal{L}_k is the segment with endpoints P_k, Q_k , it can be written as $P_k + t(Q_k - P_k)$, $0 \leq t \leq 1$. Therefore, \mathcal{L}_k has its unit tangent vector $\boldsymbol{\tau}_k = \frac{\mathbf{Q}_k - \mathbf{P}_k}{|\mathbf{P}_k - \mathbf{Q}_k|}$ and its unit normal vector $\boldsymbol{\nu}_k = i \frac{\mathbf{Q}_k - \mathbf{P}_k}{|\mathbf{P}_k - \mathbf{Q}_k|}$ in \mathbb{C} . Hence, the integral term in (3.20) can be written as

$$\begin{aligned} \int_{\mathcal{L}_k} \frac{\boldsymbol{\xi}}{\mathbf{x} - \mathbf{x}'} ds_{\mathbf{x}'} &= |\mathbf{Q}_k - \mathbf{P}_k| \int_0^1 \frac{\boldsymbol{\xi}}{(\mathbf{x} - \mathbf{P}_k) - t(\mathbf{Q}_k - \mathbf{P}_k)} dt \\ &= \frac{\boldsymbol{\xi} |\mathbf{Q}_k - \mathbf{P}_k|}{\mathbf{Q}_k - \mathbf{P}_k} \ln \frac{\mathbf{x} - \mathbf{P}_k}{\mathbf{x} - \mathbf{Q}_k}. \end{aligned}$$

From (3.21), we have

$$\begin{aligned} &\frac{\boldsymbol{\xi} |\mathbf{Q}_k - \mathbf{P}_k|}{\mathbf{Q}_k - \mathbf{P}_k} \\ &= \frac{|\mathbf{Q}_k - \mathbf{P}_k|}{\mathbf{Q}_k - \mathbf{P}_k} \left(2\Re \left\{ 1 - \frac{1}{\lambda_c(\omega)} \right\} a_{\nu_k} \frac{i(\mathbf{Q}_k - \mathbf{P}_k)}{|\mathbf{P}_k - \mathbf{Q}_k|} + 2\Re \{ \lambda_c(\omega) - 1 \} a_{\tau_k} \frac{\mathbf{Q}_k - \mathbf{P}_k}{|\mathbf{P}_k - \mathbf{Q}_k|} \right) \\ &= 2\Re \{ \lambda_c(\omega) - 1 \} a_{\tau_k} + i 2\Re \left\{ 1 - \frac{1}{\lambda_c(\omega)} \right\} a_{\nu_k}. \end{aligned}$$

Therefore, (3.20) can be simplified as

$$\Re\{\Phi(\mathbf{x})\} = \Re \left\{ \sum_{k=1}^{N_C} \mathfrak{C}_k^{\Re}(\omega, \delta_k) \ln \frac{\mathbf{x} - \mathbf{Q}_k}{\mathbf{x} - \mathbf{P}_k} + \sum_{k=1}^{N_D} \mathfrak{D}_k^{\Re}(\omega, \delta_D) \frac{1}{\mathbf{x} - \mathbf{z}_k} \right\}, \quad (3.22)$$

where $\mathfrak{C}_k^{\Re}(\omega, \delta_k)$ and $\mathfrak{D}_k^{\Re}(\omega, \delta_D)$ are the quantities defined in (3.14) and (3.16). From (3.22), the real part of Φ can be viewed as the real part of the meromorphic function $G^{\Re}(\mathbf{x})$ given by

$$G^{\Re}(\mathbf{x}) := \sum_{k=1}^{N_C} \mathfrak{C}_k^{\Re}(\omega, \delta_k) \ln \frac{\mathbf{x} - \mathbf{Q}_k}{\mathbf{x} - \mathbf{P}_k} + \sum_{k=1}^{N_D} \mathfrak{D}_k^{\Re}(\omega, \delta_D) \frac{1}{\mathbf{x} - \mathbf{z}_k}. \quad (3.23)$$

Since $G^{\Re}(\mathbf{x})$ is homomorphic except points $\mathbf{P}_k, \mathbf{Q}_k, \mathbf{z}_k$, it has complex derivative near $\partial\Omega$ in the complex plane:

$$\frac{dG^{\Re}(\mathbf{x})}{d\mathbf{x}} = \sum_{k=1}^{N_C} \mathfrak{C}_k^{\Re}(\omega, \delta_k) \left(\frac{1}{\mathbf{x} - \mathbf{Q}_k} - \frac{1}{\mathbf{x} - \mathbf{P}_k} \right) - \sum_{k=1}^{N_D} \mathfrak{D}_k^{\Re}(\omega, \delta_D) \frac{1}{(\mathbf{x} - \mathbf{z}_k)^2} \quad (3.24)$$

Similarly, we can give proof for the imaginary part of $\Phi(\mathbf{x})$. \square

The followings are remarks on Theorem 3.3:

Remark 3.4. According to Theorem 3.3, both $G^{\Re}(\mathbf{x})$ and $G^{\Im}(\mathbf{x})$ can be viewed as known quantities from the knowledge of $(-\frac{1}{2}I + \mathcal{K}_\Omega)[u^\omega - u_0]$ on $\partial\Omega$. This theorem states that $\frac{dG^{\Re}(\mathbf{x})}{d\mathbf{x}}$ is a meromorphic function in \mathbb{C} with simple poles at the endpoints $\mathbf{P}_k, \mathbf{Q}_k$ of the segments \mathcal{L}_k and poles of order 2 at the center \mathbf{z}_k of D_k . Hence, the residues of $\frac{dG^{\Re}(\mathbf{x})}{d\mathbf{x}}$ at the endpoints are given by

$$\text{Res} \left(\frac{dG^{\Re}(\mathbf{x})}{d\mathbf{x}}, \mathbf{Q}_k \right) = \mathfrak{C}_k^{\Re}(\omega, \delta_k) = -\text{Res} \left(\frac{dG^{\Re}(\mathbf{x})}{d\mathbf{x}}, \mathbf{P}_k \right). \quad (3.25)$$

The information of the center of D_k is contained in the following function

$$w(\mathbf{x}) := \sum_{k=1}^{N_D} \mathfrak{D}_k^{\Re}(\omega, \delta_D) \frac{1}{(\mathbf{x} - \mathbf{z}_k)^2}. \quad (3.26)$$

Then the function $\frac{w'(\mathbf{x})}{w(\mathbf{x})}$ will have simple poles at poles of $w(\mathbf{x})$. Hence, these center points can be identifies from boundary measurements [19].

Remark 3.5. To get some intuition of the frequency dependence of boundary data, let us look over the coefficients $\mathfrak{C}_k^{\Re}(\omega, \delta_k)$ and $\mathfrak{D}_k^{\Re}(\omega, \delta_D)$ in the formula (3.23). Recall that $\mathfrak{C}_k^{\Re}(\omega, \delta_k)$ is only related with concrete cracks \mathcal{C}_k while $\mathfrak{D}_k^{\Re}(\omega, \delta_D)$ is only related with reinforcing bars D_k . The $\lambda_c(\omega)$ in the quantity $\mathfrak{C}_k^{\Re}(\omega, \delta_k)$ satisfies

$$C_1 \frac{\sigma_c + \omega\epsilon_c}{\sigma_b + \omega\epsilon_b} \leq |\lambda_c(\omega)| \leq C_2 \frac{\sigma_c + \omega\epsilon_c}{\sigma_b + \omega\epsilon_b},$$

where C_1, C_2 are positive constants independent of ω . Since $\lim_{\delta_k \rightarrow 0} |\mathfrak{C}_k^{\Re}(\omega, \delta_k)| = 0$, the effect of the cracks at high frequencies is negligibly small. Therefore, the measured current-voltage data is mainly affected by reinforcing bars.

As frequency decreases, $|\frac{1}{\lambda_c(\omega)}|$ increases. Therefore, the quantity of term $\mathfrak{C}_k^{\Re}(\omega, \delta_k)$ becomes non-negligible. On the other hand, because $|\lambda_d(\omega)|$ does not change much with frequency, quantity of $\mathfrak{D}_k^{\Re}(\omega, \delta_D)$ varies little with respect to ω .

The above analysis show that the effect of cracks on the boundary data highly depends on frequency, while the effect of reinforcing bars doesn't depend on frequency that much. This relation leads to the results that we can detect the reinforcing bars when frequency is very high and both cracks and reinforcing bars when frequency decreases. Numerical simulations in the later part will show the verification of these analysis. We can similarly analyze $\mathfrak{C}_k^{\mathfrak{S}}(\omega, \delta_k)$ and $\mathfrak{D}_k^{\mathfrak{S}}(\omega, \delta_D)$ as above remarks. For low frequency case, instead of applying the above theorem, we have the following results.

3.4 Low-frequency case: $|\lambda_c(\omega)| \approx 0$ and $\delta_k \approx 0$ with $|\lambda_c(\omega)|^{-1}\delta_k \approx \beta$ and $0 < \beta < \infty$

In low-frequency case, the admittivity contrast $\lambda_c(\omega)$ is getting close to zero. As crack thickness δ_k goes to zero, we suppose that $\frac{1}{\lambda_c(\omega)}\delta_k \approx \beta$. Then according to lemma 3.1, potential jump along each crack could not be ignored(see Figure 2(a)). According to [1, 15, 23], we have the following asymptotic expansion formula of the potential u^ω for low frequency current.

Theorem 3.6 (Asymptotic expansion at low frequencies). *In low-frequency case, we have the following asymptotic formula for the boundary perturbations of the potential u^ω :*

$$\begin{aligned} \left(-\frac{1}{2}I + K_\Omega\right) [u^\omega - u_0](x) &= -\delta_D^2 \sum_{k=1}^{N_D} \nabla\Gamma(x, z_k) \cdot M(\lambda_d, B_k) \nabla u_0(z_k) \\ &+ \sum_{k=1}^{N_C} \int_{\mathcal{L}_k} \frac{\partial\Gamma(x, x')}{\partial\nu(x')} [u]_k(x') dx' + O(\delta_k^2) + O((\delta_D)^3). \end{aligned} \quad (3.27)$$

In this case, since the potential jump $[u^\omega]_k = 2\delta_k \frac{1}{\lambda_c(\omega)} \frac{\partial u^\omega}{\partial\nu}(x - \delta_k\nu_x)|_+$ along \mathcal{L}_k is very large and could not be ignored, the effect of reinforcing bars on the perturbations of the boundary voltage is hidden by cracks. Although we cannot write (3.27) in an explicit way, we know that it is related with the endpoints as well as the potential jump along the concrete cracks. When multiple concrete cracks are well separated from each other, we can always image them from boundary measurements. However, reinforcing bars at low frequencies are invisible since the concrete cracks will dominate the boundary measurements.

3.5 Spectroscopic analysis

Based on the above analysis in low-frequency case and high-frequency case, we mathematically derived the frequency dependency of the current-voltage

data in a rigorously way. The current-voltage data is mainly affected by the outermost cracks when frequency is low, whereas the data mainly depends on the reinforcing bars when frequency is high. With this reason, we can detect the outermost cracks at low frequency. As frequency increases, the reinforcing bars become gradually visible whereas cracks fade out (thicker crack fades out at higher frequency than thinner crack). Hence, multi-frequency EIT system allows to probe these frequency dependent behavior.

4 Numerical simulations

We make use of three different numerical simulation models on a disk $\Omega = \{(x, y) : x^2 + y^2 \leq (0.1)^2\}$ with radius unit m as shown in figure 3. We generate a finite element mesh of the disk using triangular elements. Inside the disk, we place cracks and bars. Complex admittivity distribution for each model is chosen as shown in table 1. In the numerical simulations, we

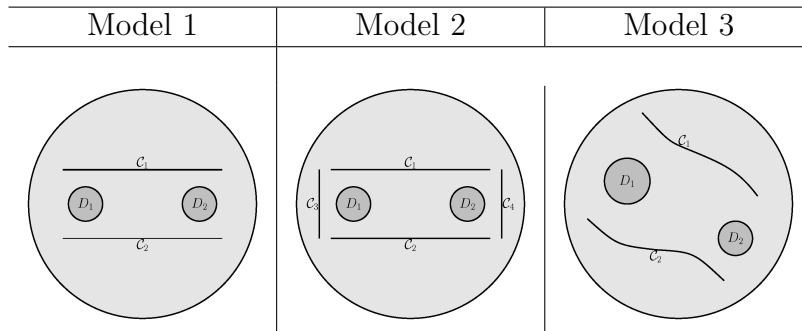


Figure 3: Models for numerical simulation.

Subdomain	Admittivity distribution
D_1, D_2	$\gamma_d^\omega = 10^5 + i\omega * 10^6 * \epsilon_0$
C_1, C_2, C_3, C_4	$\gamma_c^\omega = 10^{-6} + i\omega * 10^2 * \epsilon_0$
Otherwise	$\gamma_b^\omega = 1 + i\omega * 10^4 * \epsilon_0$

Table 1: Admittivity distribution in each subdomain ($\epsilon_0 = 8.85 * 10^{-12} F/m$)

use the standard 16-channel multi-frequency EIT system[25, 27, 32] where 16 electrodes $\mathcal{E}_1, \dots, \mathcal{E}_{16}$ are attached to $\partial\Omega$ with uniform distance between two adjacent electrodes. We inject 16 number of currents using adjacent pairs of electrodes to generate simulated current-voltage data set

$$\mathbb{F}_\omega = [V_\omega^{1,1}, \dots, V_\omega^{1,16}, V_\omega^{2,1}, \dots, V_\omega^{2,16}, \dots, V_\omega^{16,1}, \dots, V_\omega^{16,16}]^T.$$

where $V_\omega^{j,k}$ denotes the potential difference between electrodes \mathcal{E}_k and \mathcal{E}_{k+1} when the j -th current is injected using the adjacent pair \mathcal{E}_j and \mathcal{E}_{j+1} . To be precise, $V_\omega^{j,k} = u_j^\omega|_{\mathcal{E}_k} - u_j^\omega|_{\mathcal{E}_{k+1}}$ is computed by solving the following mixed boundary value problem

$$\begin{cases} \nabla \cdot (\gamma^\omega \nabla u_j^\omega) = 0 & \text{in } \Omega \\ 1 = - \int_{\mathcal{E}_j} \gamma^\omega \frac{\partial u_j^\omega}{\partial \nu} ds = \int_{\mathcal{E}_{j+1}} \gamma^\omega \frac{\partial u_j^\omega}{\partial \nu} ds \\ \nabla u_j^\omega \times \nu|_{\mathcal{E}_k} = 0, \quad \int_{\mathcal{E}_k} \gamma^\omega \frac{\partial u_j^\omega}{\partial \nu} ds = 0 \quad (k = 1, \dots, 16) \\ \gamma^\omega \frac{\partial u_j^\omega}{\partial \nu} = 0 \quad \text{on } \partial\Omega \setminus \cup_{k=1}^{16} \mathcal{E}_k, \quad \int_{\partial\Omega} u_j^\omega = 0 \end{cases} \quad (4.1)$$

where the contact impedance is ignored for simplicity. For $\omega = \omega_1, \omega_2, \dots, \omega_{N_\omega}$ ranging from 10Hz to 1MHz, we get N_ω data vectors $\mathbb{F}_{\omega_1}, \mathbb{F}_{\omega_2}, \dots, \mathbb{F}_{\omega_{N_\omega}}$. The EIT reconstruction method makes use of the sensitivity matrix \mathbb{S} :

$$\mathbb{S} = \begin{bmatrix} S_1^{1,1} & S_2^{1,1} & \dots & S_p^{1,1} & \dots & S_{N_T-1}^{1,1} & S_{N_T}^{1,1} \\ & S_1^{1,16} & S_2^{1,16} & \dots & S_p^{1,16} & \dots & S_{N_T-1}^{1,16} & S_{N_T}^{1,16} \\ & & & \vdots & & & & \\ S_1^{16,1} & S_2^{16,1} & \dots & S_p^{16,1} & \dots & S_{N_T-1}^{16,1} & S_{N_T}^{16,1} \\ & & & \vdots & & & \\ S_1^{16,16} & S_2^{16,16} & \dots & S_p^{16,16} & \dots & S_{N_T-1}^{16,16} & S_{N_T}^{16,16} \end{bmatrix}_{(16)^2 \times N_T},$$

where N_T is the number of triangular elements and

$$S_p^{j,k} = \int_{T_p} \nabla U_j(x) \cdot \nabla U_k(x) dx$$

with U_j being the solution of forward problem (4.1) with $\gamma^\omega = 1$ subject to j -th current injection between \mathcal{E}_j and \mathcal{E}_{j+1} .

We reconstruct the spectroscopic conductivity and permittivity images by solving the following linear system:

$$\mathbb{S} \delta \gamma_\omega = \mathbb{F}_\omega - \mathbb{F}_{\omega,0}$$

where $\mathbb{F}_{\omega,0}$ is the collected current-voltage data in absence of anomaly. We will describe the numerical simulations case by case.

For model 1 in figure 3, there are two reinforcing bars $D_1 = \{(x, y) : (x + 0.05)^2 + y^2 \leq (0.015)^2\}$, $D_2 = \{(x, y) : (x - 0.05)^2 + y^2 \leq (0.015)^2\}$ and two thin concrete cracks $\mathcal{C}_1 = \{(x, y) : |x| < 0.07, |y - 0.03| < 5 \times 10^{-5}\}$, $\mathcal{C}_2 = \{(x, y) : |x| < 0.07, |y + 0.03| < 2.5 \times 10^{-5}\}$. The numerical simulation in figure 4 shows that at low frequency only concrete cracks are visible; as frequency goes higher, thinner insulating crack begin to fade out whereas

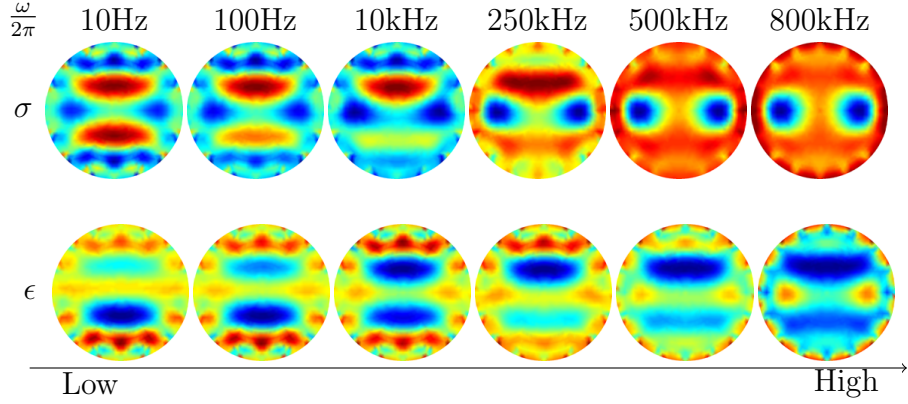


Figure 4: Reconstructed admittivity image for model 1 using 16-channel multi-frequency EIT method: the first row is σ and the second row is ϵ .

thicker crack is still visible; at high frequency, only reinforcing bars are visible.

For model 2 in figure 3, two reinforcing bars $D_1 = \{(x, y) : (x + 0.05)^2 + y^2 \leq (0.015)^2\}$, $D_2 = \{(x, y) : (x - 0.05)^2 + y^2 \leq (0.015)^2\}$ are encircled by four concrete cracks; $\mathcal{C}_1 = \{(x, y) : |x| < 0.07, |y - 0.03| < 2.5 \times 10^{-5}\}$, $\mathcal{C}_2 = \{(x, y) : |x| < 0.07, |y + 0.03| < 2.5 \times 10^{-5}\}$, $\mathcal{C}_3 = \{(x, y) : |x + 0.08| < 2.5 \times 10^{-5}, |y| < 0.03\}$, $\mathcal{C}_4 = \{(x, y) : |x - 0.08| < 2.5 \times 10^{-5}, |y| < 0.03\}$. The simulation in figure 5 shows that at low frequency, four outermost encircled cracks appear to be one object whereas reinforcing bars are hidden by cracks; as frequency increases, cracks gradually disappear whereas reinforcing bars begin to fade in.

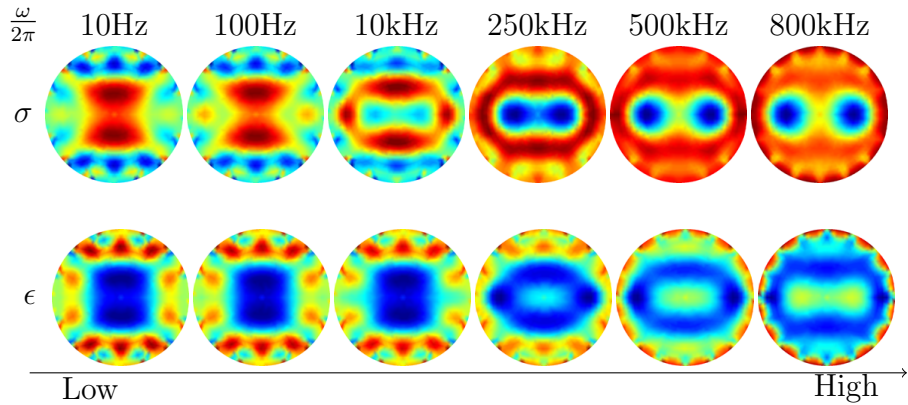


Figure 5: Reconstructed admittivity image for model 2 using 16-channel multi-frequency EIT method: the first row is σ and the second row is ϵ .

For model 3 in figure 3, there are two curved cracks with uniform thickness $5 \times 10^{-5}m$ and two reinforcing bars $D_1 = \{(x, y) : (x + 0.045)^2 + (y - 0.02)^2 \leq (0.02)^2\}$, $D_2 = \{(x, y) : (x - 0.05)^2 + (y - 0.03)^2 \leq (0.015)^2\}$. The numerical simulations in Figure 6 shows a similar behavior as in the previous simulations.

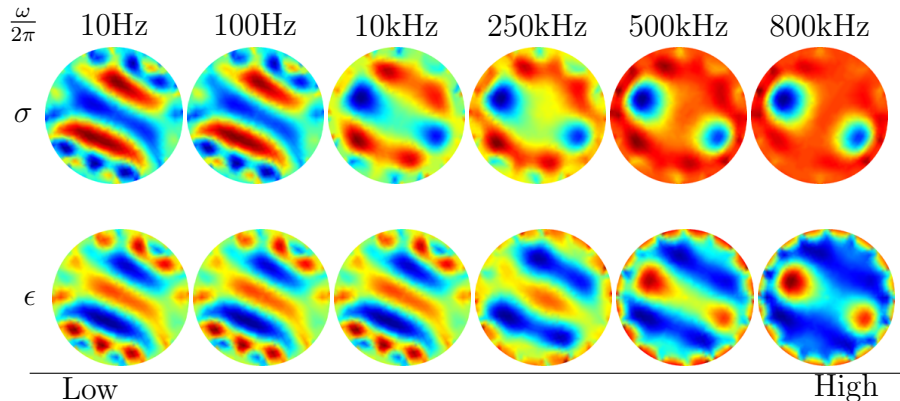


Figure 6: Reconstructed admittivity image for model 3 using 16-channel multi-frequency EIT method: the first row is σ and the second row is ϵ .

5 Conclusion

In this work, we have developed two asymptotic expansions for current-voltage data perturbations due to cracks and reinforcing bars at various frequencies. Using these two asymptotic expansions, we have mathematically shown that at high frequencies we can visualize the reinforcing bars, while at low frequencies we can only get the information of concrete cracks. Based on these mathematical analysis, we conclude that multiple frequencies help us to handle the spectroscopy behavior of the current-voltage data with respect to cracks and reinforcing bars. When the frequency increase from very low to very high, we can continuously observe the images of cracks (low frequency), both cracks and reinforcing bars (not too low, not too high frequency), and only reinforcing bars (high frequency). The mathematical results are supported by numerical illustrations.

Acknowledgements

Ammari was supported by the ERC Advanced Grant Project MULTIMOD–267184. Seo, Zhang and Zhou were supported by the National Research Foundation of Korea (NRF) grant funded by the Korean government (MEST) (No. 2011-0028868, 2012R1A2A1A03670512)

References

- [1] H. AMMARI, E. BERETTA AND E. FRANCINI, Reconstruction of thin conductivity imperfections, II. the case of multiple segments, *Appl. Anal.*, 85(2006), pp. 87-105.
- [2] H. AMMARI AND H. KANG, Reconstruction of small inhomogeneities from boundary measurements, *Lecture Notes in Math.* 1846, Springer-Verlag, Berlin, 2004.
- [3] H. AMMARI AND H. KANG, Polarization and moment tensors with applications to inverse problems and effective medium theory, *Appl. Math.Sci.*, Springer-Verlag, New York, 2007.
- [4] H. AMMARI, H. KANG AND E. KIM, Detection of internal corrosion, *ESAIM Proc.*, 26(2009), pp. 207-216.
- [5] H. AMMARI, H. KANG, E. KIM, H. LEE AND K. LOUATI, Vibration testing for detecting internal corrosion, *Stud. Appl. Math.*, 122(2009), pp. 85-104.
- [6] H. AMMARI, H. KANG, E. KIM, M. LIM AND K. LOUATI, A direct algorithm for ultrasound imaging of internal corrosion, *SIAM J. Numer. Anal.*, 49(2011), pp. 1177-1193.
- [7] H. AMMARI, H. KANG, E. KIM, K. LOUATI AND M. S. VOGELIUS, A music-type algorithm for detecting internal corrosion from electrostatic boundary measurements, *Numer. Math.*, 108(2008), pp. 501-528.
- [8] E. BERETTA, E. FRANCINI AND M. S. VOGELIUS, Asymptotic formulas for steady state voltage potentials in the presence of thin inhomogeneities. a rigorous error analysis, *J. Math. Pures Appl.*, 82(2003), pp. 1277-1301.
- [9] E. BERETTA, A. MUKHERJEE AND M. S. VOGELIUS, Asymptotic formulas for steady state voltage potentials in the presence of conductivity imperfections of small area, *Z. Angew. Math. Phys.*, 52(2001), pp. 543-572.

- [10] M. BUETTNER, A. RAMIREZ AND W. DAILY, Electrical resistance tomography for imaging concrete structures, Structural materials technology an NDT conference, San Diego, C.A., U.S., 1996.
- [11] M. CHOUREAU AND S. BEAULIEU, An investigation on application of the electrical resistivity tomography method to concrete structures, Geophysics, Los Angeles, CA, USA, 2002.
- [12] C. COLLA, D. MCCANN, P. DAS AND M. C. FORDE, Investigation of a stone masonry bridge using electromagnetics, evaluation and strengthening of existing masonry structures, RILEM, pp. 163-172, 1995.
- [13] J. L. DAVIS AND A. P. ANNAN, Ground penetrating radar for high-resolution mapping of soil and rock stratigraphy, Geophys. Prospect., 37(1989), pp. 531-551.
- [14] G. G. DIAMOND, D. A. HUTCHINS, T. H. GAN, P. PURNELL AND K. K. LEONG, Single-sided capacitive imaging for NDT, Insight, 48(2006), pp. 724-730.
- [15] A. FRIEDMAN AND M. S. VOGELIUS, Identification of small inhomogeneities of extreme conductivity by boundary measurements: a theorem on continuous dependence, Arch. Rational Mech. Anal., 105(1989), pp. 299-326.
- [16] C. GERARD AND P. E. FELDMANN, Non-destructive testing of reinforced concrete, Structural Testing, (2008), pp. 13-17.
- [17] T. C. HOU AND J. P. LYNCH, Tomographic imaging of crack damage in cementitious structural components, 4th International Conference on Earthquake Engineering, Taipei, Taiwan, 2006, pp. 1-10.
- [18] I.A.E.A., Guidebook on non-destructive testing of concrete structures, Training Course Serise No. 17, Int. Atomic Energy Agency, Austria, 2002.
- [19] H. KANG AND H. LEE, Identification of simple poles via boundary measurements and an application of EIT, Inverse Problems, 20(2004), pp. 1853-1863.
- [20] K. KARHUNEN, A. SEPPÄNEN, A. LEHIKONEN, J. BLUNT, J. P. KAIPIO AND P. J. M. MONTEIRO, Electrical resistance tomography for assessment of cracks in concrete, ACI Mat. J., 107(2010), pp. 523-531.

- [21] K. KARHUNEN, A. SEPPÄNEN, A. LEHIKONEN, J. P. KAIPIO AND P. J. M. MONTEIRO, Locating reinforcing bars in concrete with electrical resistance tomography, *Concrete Repair, Rehabilitation and Retrofitting II*-Alexander et al. (eds), Taylor & Francis Group, 2009.
- [22] K. KARHUNEN, A. SEPPÄNEN, A. LEHIKONEN, P. J. M. MONTEIRO AND J. P. KAIPIO, Electrical resistance tomography imaging of concrete, *Cement and Concrete Research*, 40(2010), pp. 137-145.
- [23] A. KHELIFI AND H. ZRIBI, Asymptotic expansions for the voltage potentials with two-dimensional and three-dimensional thin interfaces, *Math. Meth. Appl. Sci.*, 34(2011), pp. 2274-2290.
- [24] S. KIM, E. J. LEE, E. J. WOO AND J. K. SEO, Asymptotic analysis of the membrane structure to sensitivity of frequency-difference electrical impedance tomography, *Inverse Problems*, 28(2012).
- [25] S. KIM, J. LEE, J. K. SEO, E. J. WOO AND H. ZRIBI, Multifrequency trans-admittance scanner: mathematical framework and feasibility, *SIAM J. Appl. Math.*, 69(2008), pp. 22-36.
- [26] D. M. McCANN AND M. C. FORDE, Review of ndt methods in the assessment of concrete and masonry structures, *NDT&E Int.*, 34(2001), pp. 71-84.
- [27] T. I. OH, J. LEE, J. K. SEO, S. W. KIM AND E. J. WOO, Feasibility of breast cancer lesion detection using a multi-frequency trans-admittance scanner (TAS) with 10 Hz to 500 kHz bandwidth, *Physiol. Meas.*, 28(2007), pp. S71-S84.
- [28] C. POIGNARD, Asymptotics for steady-state voltage potentials in a bidimensional highly contrasted medium with thin layer, *Math. Meth. Appl. Sci.*, 31(2007), pp. 443-479.
- [29] C. POIGNARD, About the transmembrane voltage potential of a biological cell in time-harmonic regime, *ESAIM Proc.*, 26(2009), pp. 162-179.
- [30] M. SANSALONE AND N. J. CARINO, Impact-echo method: detecting honeycombing, the depth of surface-opening cracks, and ungrouted ducts, *Concrete Int.: Design and Cons.*, 10(1988), pp. 38-46.
- [31] M. SANSALONE AND N. J. CARINO, Impact-echo: a method for flaw detection in concrete using transient stress waves, Rep. No. NBSIR 86-3452, National Bureau of Standards, Gaithersburg, Md., 1986.

- [32] J. K. SEO AND E. J. WOO., Nonlinear inverse problems in imaging, John Wiley & Sons, 2012.
- [33] E. M. STEIN AND R. SHAKARCHI, Complex analysis, Princeton University Press, 2003.
- [34] X. YIN, D. A. HUTCHINS, G. G. DIAMOND AND P. PURNELL, Non-destructive evaluation of concrete using a capacitive imaging technique: preliminary modelling and experiments, Cement and Concrete Research, 40(2010), pp. 1734-1743.